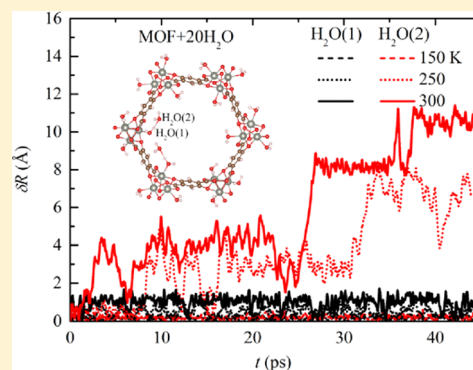


# H<sub>2</sub>O Adsorption/Desorption in MOF-74: *Ab Initio* Molecular Dynamics and Experiments

Yunsong Li,<sup>†</sup> Xinjiang Wang,<sup>†</sup> Dongyan Xu,<sup>‡</sup> Jae Dong Chung,<sup>§</sup> Massoud Kaviani,<sup>||</sup> and Baoling Huang<sup>\*†</sup><sup>†</sup>Department of Mechanical and Aerospace Engineering, Hong Kong University of Science and Technology, Kowloon, Hong Kong<sup>‡</sup>Department of Mechanical and Automation Engineering, Chinese University of Hong Kong, Shatin, Hong Kong<sup>§</sup>Department of Mechanical Engineering, Sejong University, Seoul 143-747, Republic of Korea<sup>||</sup>Department of Mechanical Engineering, University of Michigan, Ann Arbor, Michigan 48109, United States

**ABSTRACT:** Using density functional theory based molecular dynamics with the tight-binding approximation and experimental characterization, the H<sub>2</sub>O vapor adsorption/desorption processes in Zn-MOF-74 and the corresponding influence on the lattice dynamics were investigated. It was found that the Zn sites are preferred for H<sub>2</sub>O adsorption, and they even allow for the adsorption of multiple H<sub>2</sub>O molecules on the same site, making it possible to form stable H<sub>2</sub>O cluster at low temperatures. The adsorption heats of different adsorption processes were predicted, and the possibility of H<sub>2</sub>O cluster formation under vapor exposure at low and room temperatures was explored. The first adsorbed H<sub>2</sub>O can only be dissociated at elevated temperatures, therefore reducing the cyclic uptake near the room temperature. The vibrational spectra of the lattice and adsorbed H<sub>2</sub>O were also calculated using molecular dynamics simulation to illuminate the variation of lattice dynamics during the adsorption. The framework was found to be stable after water vapor exposure near room temperature but may start to collapse at around 570 K. X-ray diffraction and H<sub>2</sub>O adsorption isotherm measurements have been conducted to verify the theoretical predictions, and good agreements are found.



## 1. INTRODUCTION

H<sub>2</sub>O adsorption in micro- and mesoporous solids has gained renewed interest for its great potential applications in sorption heat transformation systems.<sup>1–5</sup> As an alternative to conventional vapor-compression-driven systems, thermally driven adsorption chillers (TDCs) or adsorption heat pumps (AHPs) based on H<sub>2</sub>O adsorption/desorption provide a more efficient and environmentally friendly approach for harvesting low-temperature heat.<sup>6</sup> Silica gel and zeolites have been widely utilized, but they have many disadvantages.<sup>7</sup> For example, zeolites have a high affinity for H<sub>2</sub>O, adsorbing well at a low relative pressure (or humidity) of  $P/P_0 = 0.001–0.01$  but requiring high desorption temperatures (typically over 600 K), and they also have a low H<sub>2</sub>O loading about 0.05–0.46 g/g.<sup>8</sup> Silica gels are less hydrophilic than zeolites and require lower desorption temperatures (typically around 400 K) but also have low cyclic H<sub>2</sub>O exchange. Search continues for adsorbents with large H<sub>2</sub>O uptake, sharp increase in H<sub>2</sub>O uptake at low/medium humidity, desorption at low temperatures, and high structural stability.<sup>9,10</sup>

Metal–organic frameworks (MOFs) are crystalline porous solids composed of inorganic building units and organic linkers. The dimensions and environments of the pores can be easily tuned by changing the combination of inorganic and organic units. MOFs have been utilized as adsorbents for a range of guest molecules in various applications,<sup>11,12</sup> including gas storage (e.g., H<sub>2</sub>, CO<sub>2</sub>, and CH<sub>4</sub>)<sup>13,14</sup> and separation (e.g.,

carbon capture from flue gas and natural gas sweetening).<sup>15–19</sup> The unique features of MOFs such as huge surface area, large pore volume, and physicochemical variability make them promising candidates for water-based sorption heat transformation applications, in which excellent hydrothermal stability is required. Recently, water-stable MOFs have been developed for industrial applications involving H<sub>2</sub>O adsorption and release.<sup>20–23</sup> For example, Cr-MIL-101 exhibits large H<sub>2</sub>O uptake capacity (1.4 g/g at 300 K), and high desorption rates below 350 K; however, relatively high relative pressure ( $0.40 < P/P_0 < 0.54$ ) is required to adsorb H<sub>2</sub>O.<sup>4</sup>

To reduce the condensation pressure, it is preferable to reduce the pore diameter in addition to the introduction of strong water binding sites.<sup>24,25</sup> For instance, M-MOF-74 [ $M_2(\text{DOT})$ , DOT = 2,5-dioxidoterephthalate, M = Zn, Mg, Co, and Ni] with coordinatively unsaturated metal sites (Lewis acidic sites) has demonstrated high H<sub>2</sub>O uptake under low relative pressure ( $P/P_0 < 0.3$ );<sup>24,26–28</sup> e.g., Mg-MOF-74 can take up 0.54 g/g of H<sub>2</sub>O below 10% relative humidity.<sup>27,29</sup> However, there exist challenges in regeneration of the material under mild conditions. Indeed, a significant surface area drop of Mg-MOF-74 has been observed after exposure to water.<sup>27,29</sup> The mechanism for this degradation has been under debate for

Received: March 3, 2015

Revised: May 10, 2015

Published: May 12, 2015

**Table 1.** Zn-MOF-74 Lattice Parameters, Unit Cell Volumes ( $V_c$ ), Average Distance between Zn<sup>2+</sup> Site and O in H<sub>2</sub>O ( $R_{Zn-OH_2}$ ), Average Adsorption Energy per H<sub>2</sub>O ( $\Delta E_1$ ), and Adsorption Energy of H<sub>2</sub>O on the Secondary Sites ( $\Delta E_2$ ), under Variable H<sub>2</sub>O Load (Volume Changes Are Shown in Parentheses)

adsorption sites	loading	method	lattice constant (Å)			angle (deg)			$V_c$ (Å <sup>3</sup> (fu) <sup>-1</sup> )	$R_{Zn-OH_2}$ (Å)	$\Delta E_1$ (eV)	$\Delta E_2$ (eV)
			$a$	$b$	$c$	$\alpha$	$\beta$	$\gamma$				
primary	0	Exp <sup>47</sup>	25.932	25.932	6.837	90	90	120	3981.5			
		DFT	26.156	26.156	6.556	90	90	120	3884.0 (-2.45%)			
		DFTB	25.824	25.829	6.720	90	90	120	3880.9 (-2.53%)			
	1	DFT	26.133	26.303	6.529	90.2	89.8	120.1	3882.7 (-0.13%)	2.223	-0.67	
		DFTB	25.687	25.913	6.720	90.1	90	119.7	3883.7 (0.07%)	2.234	-0.70	
		DFT	25.960	26.020	6.884	89.9	90	120	4046.1 (4.17%)	2.229	-0.66	
secondary	18	DFTB	26.263	26.186	6.753	90	90	119.9	4026.5 (3.75%)	2.239	-0.65	
		DFTB	25.632	25.954	6.718	90.1	90	119.6	3884.6 (0.10%)	2.208 <sup>a</sup>	-0.55	-0.41
		DFTB	26.228	26.247	6.750	90	90	120	4026.3 (3.75%)	2.205 <sup>a</sup>	-0.63	-0.41
	20	DFTB	26.266	26.277	6.748	90	90	120.	4033.8 (3.94%)	2.203 <sup>a</sup>	-0.62	-0.41

<sup>a</sup>Vicinity of H<sub>2</sub>O at a secondary site.

a long time while recently Tan et al. attributed it to the water reaction with the host at high temperatures.<sup>1</sup> The gas-adsorption capacity of MOF-74 is also significantly influenced by humidity,<sup>30</sup> highlighting the importance of fundamental understanding of the H<sub>2</sub>O adsorption/desorption process in MOF-74. Besides, whether or how H<sub>2</sub>O uptake might influence the MOF-74 lattice structure and its properties is a concern in many applications, while a recent classical molecular dynamic prediction reports that high H<sub>2</sub>O adsorption will destabilize the MOF-74 structure.<sup>31</sup>

In this work, we select Zn-MOF-74, of which a high H<sub>2</sub>O uptake capacity is reported to be 0.32 g/g,<sup>30</sup> as an example to explore the H<sub>2</sub>O adsorption/desorption processes in MOF-74 and their influence on the structural stability and lattice dynamics of MOF-74. By using first-principles calculations, the preferential H<sub>2</sub>O adsorption sites are identified, and the corresponding adsorption heats are predicted. *Ab initio* MD has been used to illuminate the influence of H<sub>2</sub>O adsorption on lattice vibration as well as the variation of H<sub>2</sub>O adsorption/desorption in Zn-MOF-74 structure with respect to the progressively increasing water loading and temperature. Experimental characterizations, including powder X-ray diffraction (PXRD) analysis and nitrogen and H<sub>2</sub>O adsorption measurements, have also been carried out for the comparison. It is found that Zn-MOF-74 structure remains stable near room temperature even under high H<sub>2</sub>O uptake. The open Zn sites are the preferred adsorption sites, which also allow for the adsorption of multiple H<sub>2</sub>O molecules. The first absorbed H<sub>2</sub>O on the primary sites can only be dissociated at elevated temperatures, which may screen the Zn sites and reduce the cyclic uptake of other guest molecules near room temperature.

## 2. THEORETICAL AND EXPERIMENTAL METHODS

**2.1. DFTB Computations.** The calculations in this work were performed using the density-functional-based tight-binding (DFTB) method implemented in the DFTB+ code,<sup>32</sup> which is a fast and efficient quantum mechanical simulation method based on a second-order expansion of the Kohn–Sham total energy in density functional theory (DFT)<sup>33,34</sup> with respect to charge density fluctuations. The DFTB approach, originally suggested for periodic systems,<sup>35</sup> has been mainly developed in refs 36–40. DFTB is about 3 orders of magnitude faster than DFT, comparable to the semiempirical methods,<sup>40</sup> making it suitable for large systems where the conventional *ab*

*initio* quantum chemistry calculations are often prohibitive. So, it is balance between computational efficiency and accuracy, required for the large MOF systems, which are computationally demanding for the traditional DFT methods. Both the mio-1-1<sup>36</sup> and Znorg-0-1<sup>41</sup> parameter sets are used. The mio set was developed for organic molecules with atoms including O, N, C, and H, while the Znorg set is developed with a focus on the interactions between Zn and common atoms in organic molecules, i.e., Zn–X (X = C, H, N, O, S, and Zn).

During the optimization, the periodic boundary conditions were used, and the cell shape, volume, and atomic positions were relaxed until a maximum force component of 10<sup>-6</sup> au was achieved. The Brillouin zone was sampled with a 6 × 6 × 6 mesh including the  $\Gamma$  point. Since the van der Waals interactions involved are long-range interactions, to avoid “self-interactions” in a small simulation domain, a large hexagonal Zn-MOF-74 unit cell including 18 Zn<sup>2+</sup> ions and 9 DOT linkers was used for all the DFTB calculations. The SCC-DFTB calculations were also performed on isolated H<sub>2</sub>O molecules in 20 Å boxes. The Lennard-Jones dispersion model was used to correct van der Waals interactions.<sup>42</sup> For the DFTB molecular dynamic (MD) simulations, the optimized geometry of the most stable structure was used for the initial positions of atoms; the initial velocities of atoms were given at random, satisfying the mean kinetic temperature requirement. The velocities and positions of atoms during in MD were computed by the velocity-Verlet algorithm.<sup>43,44</sup> The step times were 1 fs under the *NPT* ensemble (constant number of particles, pressure, and temperature) at 1 atm using the Berendsen thermostat and brostat with 1 fs and 4 ps damping constants, respectively.

**2.2. vdW DFT Calculations.** To verify the accuracy of the simulation of H<sub>2</sub>O adsorption in the cavities of the Zn-MOF-74 by the DFTB method, we also used DFT calculations with the vdW (van der Waals)-DF exchange-correlation functional,<sup>45–47</sup> as implemented in the Vienna *Ab initio* Simulation Package (VASP).<sup>48–50</sup> This particular exchange-correlation functional is capable of capturing van der Waals interactions, which play an important role in H<sub>2</sub>O adsorption in MOFs, and it has been applied successfully to the study of the adsorption of small molecules in MOF materials.<sup>25,51</sup> Convergence with respect to both energy cutoff and  $k$ -point mesh has been tested. As a result of the convergence, an energy cutoff of 600 eV was chosen to ensure that the total energies were converged within

1.0 meV (fu)<sup>-1</sup>. The Brillouin zone was sampled with a mesh including the gamma point. A 2 × 2 × 2 *k*-point is selected for full structural relaxation using the Gaussian smearing method,<sup>52</sup> and a smearing parameter of 0.1 eV was chosen such that the error in the extrapolated energy at 0 K was less than 1.0 meV (fu)<sup>-1</sup>. The final energies for the optimized geometries were recalculated by using the tetrahedron method with Blöchl corrections. The absorption energies from this method are taken as a reference for comparison with calculated absorption energies using the DFTB method.

**2.3. Comparison between DFTB and DFT.** To evaluate the accuracy of the DFTB method, we first used DFT calculations with the vdW-DF,<sup>45–47</sup> as implemented in the VASP,<sup>48–50</sup> to calculate the structural parameters and the average adsorption energies per H<sub>2</sub>O on the primary adsorption sites, which serve as benchmark calculations. After the full relaxation of a MOF structure with *n* H<sub>2</sub>O molecules uniformly distributed near the adsorption sites (see the discussion in section 3.1), the average adsorption energy per H<sub>2</sub>O ( $\Delta E_1$ ) and adsorption energy of H<sub>2</sub>O on the secondary sites ( $\Delta E_2$ ) for variable loads are determined from

$$\Delta E_1 = \frac{1}{n} \{E(\text{MOF} + n\text{H}_2\text{O}) - [E(\text{MOF}) + nE(\text{H}_2\text{O})]\} \quad (1)$$

$$\Delta E_2 = \{E(\text{MOF} + n\text{H}_2\text{O}) - [E(\text{MOF} + (n - 1)\text{H}_2\text{O}) + E(\text{H}_2\text{O})]\} \quad (2)$$

where  $E(\text{MOF} + n\text{H}_2\text{O})$  and  $E(\text{MOF} + (n - 1)\text{H}_2\text{O})$  are the internal energies of the Zn-MOF-74 with *n* and (*n* - 1) adsorbed H<sub>2</sub>O, respectively,  $E(\text{MOF})$  and  $E(\text{H}_2\text{O})$  are the internal energies of the empty Zn-MOF-74 and H<sub>2</sub>O in their fully relaxed structure, and *n* is the number of the adsorbed H<sub>2</sub>O. As shown in Table 1, the lattice parameters and unit cell volumes ( $V_c$ ) of Zn-MOF-74 obtained by DFT and DFTB are in good agreement with experimental data (about 2.5% volume difference).<sup>53</sup> For the variable H<sub>2</sub>O loadings such as 1, 2, and 18, the lattice parameters, unit cell volumes (at most 0.6% difference), and  $\Delta E_1$  (at most 0.03 eV difference) obtained by DFTB are in good agreement with those by the DFT method, indicating that the DFTB method can replace DFT with the vdW-DF method to study the adsorption properties of H<sub>2</sub>O in Zn-MOF-74. Therefore, we would use the DFTB method instead of DFT in the further study to enhance computational efficiency.

**2.4. IR Spectra and VDOS Calculations.** The infrared (IR) absorption spectrum is obtained by the Fourier transformation of the dipole moment autocorrelation function, i.e.<sup>54</sup>

$$I(\omega) \propto \int_0^\infty \left\langle \frac{dp_e(t)}{dt} \frac{dp_e(0)}{dt} \right\rangle \cos(\omega t) dt \quad (3)$$

where  $I(\omega)$  is the spectral intensity,  $p_e(t)$  is the total electric dipole moment at time *t*, and  $\omega$  is the vibration frequency. The time derivative of the dipole moment is

$$\frac{dp_e(t)}{dt} = \sum_{i=1}^n q_i \frac{dr_i(t)}{dt} = \sum_{i=1}^n q_i v_i(t) \quad (4)$$

where  $q_i$ ,  $r_i$ , and  $v_i$  are the partial charge, position and velocity of atom *i*. The partial charges were obtained based on the Bader population analysis.

The vibrational density of states (VDOS),  $D(\omega)$ , is obtained by the Fourier transformation of the velocity autocorrelation function, i.e.<sup>54</sup>

$$D(\omega) \propto \int_0^\infty \Gamma(t) \cos(\omega t) dt \quad (5)$$

Here

$$\Gamma(t) = \sum_i^n \langle \mathbf{u}_i(t) \cdot \mathbf{u}_i(0) \rangle / \sum_i^n \langle \mathbf{u}_i(0) \cdot \mathbf{u}_i(0) \rangle \quad (6)$$

where  $\mathbf{u}_i$  is the velocity of atom *i*.

**2.5. Materials Synthesis.** H<sub>4</sub>DOT and *N,N*-dimethylformamide (DMF) were obtained from Aldrich. Zinc nitrate hexahydrate [Zn(NO<sub>3</sub>)<sub>2</sub>·6H<sub>2</sub>O] was purchased from Fisher Scientific. All starting materials and solvents were used without further purification. Zn-MOF-74 was prepared and activated according to the published procedure.<sup>24</sup>

**2.6. Materials Characterization.** PXRD patterns were recorded on a Bruker D8 Advance diffractometer (Göbel mirror monochromated Cu K $\alpha$  radiation  $\lambda = 1.54056 \text{ \AA}$ ). Attenuated total reflectance Fourier transform infrared (ATR-FTIR) spectra were recorded on a Bruker ALPHA FT-IR spectrometer equipped with an ATR sampling module. Thermal gravimetric analysis (TGA) measurements were performed using a TA Instruments SDT-Q600 thermogravimetric analyzer at a heating rate of 5 °C/min under N<sub>2</sub> flow. Low-pressure N<sub>2</sub> adsorption isotherms were recorded on a Quantachrome Autosorb-1 or Quantachrome Quadrasorb-SI volumetric gas adsorption analyzers. H<sub>2</sub>O isotherms were measured on a BELSORP-aqua3 (BEL Japan).<sup>26</sup> Helium was used for the estimation of dead space for N<sub>2</sub> and H<sub>2</sub>O adsorption measurements. Ultrahigh-purity grade N<sub>2</sub> and He gases (Praxair, 99.999% purity) were used for the TGA and gas adsorption experiments.

### 3. RESULTS AND DISCUSSION

**3.1. Adsorption Energies and Structure Dependence on H<sub>2</sub>O Loadings.** Zn-MOF-74 is composed of Zn<sup>2+</sup> ions and DOT linkers, as shown in Figure 1a. Each Zn<sup>2+</sup> ion is coordinated with six oxygen atoms: five from the linkers and one from a guest molecule (typically H<sub>2</sub>O or DMF).<sup>53</sup> The edges of adjacent ZnO<sub>6</sub> octahedra are shared to construct the 1-D rod inorganic secondary building unit (SBU), [Zn<sub>3</sub>O<sub>3</sub>(CO<sub>2</sub>)<sub>3</sub>]<sub>∞</sub>, and these 1-D rods are bridged by DOT linkers to create a 1-D hexagonal channel along the *c*-axis.<sup>53</sup> The overall Zn-MOF-74 [Zn<sub>18</sub>(DOT)<sub>9</sub>(guest)<sub>18</sub>] structure is built in  $R\bar{3}$  symmetry, in which a hexagonal unit cell includes 18 Zn<sup>2+</sup> ions and 9 DOT linkers. The coordinated guest molecules on Zn<sup>2+</sup> ions can be removed to produce coordinated unsaturated Zn sites (open metal sites).

To find all possible adsorption sites for H<sub>2</sub>O, we calculated the binding energy distribution of H<sub>2</sub>O throughout the cavity. According to the symmetries, the cavity was divided into six equivalent triangular regions defined by the center of cavity and two adjacent Zn<sup>2+</sup> sites (Figure 1b). The normal vector of the plane makes a 16.65° with the channel direction (because of the two adjacent Zn<sup>2+</sup> sites). In order to calculate the binding energy distribution of H<sub>2</sub>O throughout the cavity, 28 equidistant points within this plane were sampled, and linear interpolation was used to construct the binding energy map. At each point, the oxygen atom of H<sub>2</sub>O was placed to the location of interest, and the center of mass in the Zn-MOF-74 unit cell

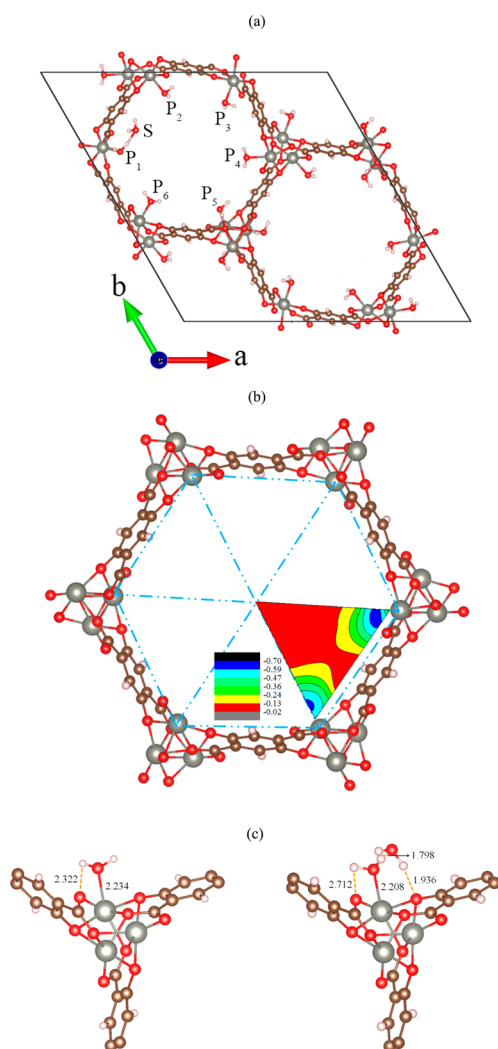


**Figure 1.** (a) Unit-cell structural model of Zn-MOF-74 with the adsorbed  $\text{H}_2\text{O}$  viewed along the  $c$ -axis direction, where the primary adsorption sites denoted as P and the secondary adsorption site denoted as S. (b) A map of the binding energy distribution as the  $\text{H}_2\text{O}$  molecule moved throughout the cavity of Zn-MOF-74 viewed along the  $c$ -axis direction. (c) Optimized structures of the Zn-MOF-74 cluster with the adsorbed  $\text{H}_2\text{O}$  on the primary site in MOF +  $\text{H}_2\text{O}$  (left) and on the secondary site in MOF +  $2\text{H}_2\text{O}$  (right). Atom colors: C = black, O = red, H = white, Zn = large gray.

was fixed while the remaining atoms were allowed to relax (so the molecule adopts its lowest energy orientation and internal geometry).

Figure 1b shows the binding energy distribution for one  $\text{H}_2\text{O}$ . The largest binding energy is found in the region close to the  $\text{Zn}^{2+}$  ion, while near the center of cavity and the center of two adjacent  $\text{Zn}^{2+}$  ions the binding energies are the smallest, i.e.,  $-0.02$  eV. Therefore,  $\text{H}_2\text{O}$  molecules will move to the  $\text{Zn}^{2+}$  site after the coordinate relaxation no matter where the initial locations of  $\text{H}_2\text{O}$  molecules are, leading to the fact that the primary adsorption sites lie on a corner of the hexagonal 1D channel created by the  $\text{Zn}^{2+}$  ion. This binding energy distribution is very similar to the results reported for Mg-MOF-74,<sup>55</sup> wherein the binding energy on the primary sites is slightly larger in Mg-MOF-74. When a  $\text{H}_2\text{O}$  molecule is adsorbed at a primary site and a second  $\text{H}_2\text{O}$  molecule is placed in the triangle region, the second  $\text{H}_2\text{O}$  molecule will move

toward the first  $\text{H}_2\text{O}$  molecule at the primary adsorption site and become stabilized next to the first  $\text{H}_2\text{O}$  molecule. This indicates the existence of secondary adsorption sites in Zn-MOF-74. For convenience, we denote the  $\text{H}_2\text{O}$  molecules at the primary and secondary adsorption sites as  $\text{H}_2\text{O}(1)$  and  $\text{H}_2\text{O}(2)$ , respectively.

In order to identify the exact positions and orientations of the adsorbed  $\text{H}_2\text{O}$  molecules on the primary and secondary sites in Zn-MOF-74, two Zn-MOF-74 structures with different  $\text{H}_2\text{O}$  loadings were fully optimized. In the first structure (denoted as MOF +  $\text{H}_2\text{O}$ ),  $\text{H}_2\text{O}(1)$  was adsorbed at a primary site  $\text{P}_1$  in Figure 1a while in the second (denoted as MOF +  $2\text{H}_2\text{O}$ ) one  $\text{H}_2\text{O}(1)$  and one  $\text{H}_2\text{O}(2)$  were adsorbed at a primary  $\text{P}_1$  and a secondary site S in Figure 1a, respectively. During the optimization, all the atoms of Zn-MOF-74 and the adsorbed  $\text{H}_2\text{O}$  molecules were allowed to relax. The detailed geometries of the Zn-MOF-74 inorganic unit with the adsorbed  $\text{H}_2\text{O}$  on the primary and secondary sites are shown in Figure 1c. For the  $\text{H}_2\text{O}(1)$  molecule on the primary site, the center-to-center distance between Zn and O in  $\text{H}_2\text{O}(1)$  ( $R_{\text{Zn}-\text{OH}_2}$ ) is 2.234 Å, which is slightly larger than that from the XRD data (2.119 Å) of Zn-MOF-74 (Zn-CPO-27)<sup>56</sup> and is only slightly larger than the average Zn–O bond length of 2.110 Å in  $\text{ZnO}_5$  moiety. Also, the hydrogen atoms of  $\text{H}_2\text{O}(1)$  molecule lean toward carboxylate oxygen atoms, and the distance between O in MOF and H in  $\text{H}_2\text{O}(1)$  is 2.322 Å, a typical length for a hydrogen bond (1.5–2.5 Å). Therefore, there exist two types of interactions, i.e., Zn–O bonding and hydrogen bonding interactions, between MOF and the adsorbed  $\text{H}_2\text{O}(1)$  molecule on the primary sites.

With a  $\text{H}_2\text{O}(2)$  adsorbed on the secondary site, the distance between Zn and O in the  $\text{H}_2\text{O}(1)$  is shortened to 2.208 Å, while the distance between O in MOF and H in the  $\text{H}_2\text{O}(1)$  molecule is lengthened to 2.712 Å (Figure 1c). These indicate that the stabilization of  $\text{H}_2\text{O}(2)$  molecule in the framework reinforces the Zn–O bonding interactions but weakens the hydrogen-bonding interactions between the  $\text{H}_2\text{O}(1)$  molecule and MOF. Furthermore, the hydrogen atoms of the  $\text{H}_2\text{O}(2)$  molecule also lean toward the carboxylate oxygen atoms, and the distance between O in MOF and H in  $\text{H}_2\text{O}(2)$  is 1.936 Å, far smaller than the distance between O in MOF and H in  $\text{H}_2\text{O}(1)$  (2.322 Å). This indicates that there is a hydrogen-bonding interaction between  $\text{H}_2\text{O}(2)$  and the MOF framework, which is even stronger than that for  $\text{H}_2\text{O}(1)$  on the primary site. Meanwhile, the distance between H in  $\text{H}_2\text{O}(1)$  and O in  $\text{H}_2\text{O}(2)$  is 1.798 Å, similar to the H–O bond length ( $\sim 1.8$  Å) in a  $\text{H}_2\text{O}$  molecule. This means that  $\text{H}_2\text{O}(2)$  will also bond with the first  $\text{H}_2\text{O}(1)$  through a hydrogen bond.

In order to explore the effects of higher  $\text{H}_2\text{O}$  loadings on the Zn-MOF-74 structure under different water loadings (18–20  $\text{H}_2\text{O}$  molecules), the lattice parameters and unit cell volumes were calculated and compared to those of aforementioned MOF +  $\text{H}_2\text{O}$  and MOF +  $2\text{H}_2\text{O}$  structures. Since each unit cell contains 18 Zn primary sites, it is likely that first 18  $\text{H}_2\text{O}$  molecules will stay next to these Zn sites (denoted as MOF +  $18\text{H}_2\text{O}$ ). The models containing one and two extra  $\text{H}_2\text{O}$  molecules are also created (denoted as MOF +  $19\text{H}_2\text{O}$  and MOF +  $20\text{H}_2\text{O}$ , respectively), where these water molecules should be stabilized at the secondary adsorption site. The lattice parameters and unit cell volume are slightly influenced by the  $\text{H}_2\text{O}$  loading. Similar conclusion has been drawn by Canepa et al.,<sup>57</sup> although they only reported a small volume contraction

with the load of 6 H<sub>2</sub>O molecules. As listed in Table 1, for one H<sub>2</sub>O per unit cell, DFT results show that the cell volume slightly decreases by 0.04%. When H<sub>2</sub>O molecules occupy all the primary sites (18 H<sub>2</sub>O per unit cell), the cell volume increases by 3.8%, and after the occupation of the secondary sites, such as 20 H<sub>2</sub>O per unit cell, it increases by 4.0%. This is normal since for a small loading the host–guest attractive dispersive interactions dominate while for a larger loading the short-range repulsive interactions become more important.<sup>58</sup> However, the variation of the distance between Zn and O (in H<sub>2</sub>O(1)) is rather modest (<0.2%) even when the amount of H<sub>2</sub>O loading increases. The adsorption energies of H<sub>2</sub>O in Zn-MOF-74 ( $\Delta E$ ) are also dependent on the loading, and with one H<sub>2</sub>O per unit cell, the  $\Delta E_1$  is  $-0.70$  eV ( $-67.5$  kJ/mol). With H<sub>2</sub>O on all primary sites (MOF + 18H<sub>2</sub>O),  $\Delta E_1$  decreases to  $-0.65$  eV, and this difference is associated with the intermolecular repulsions between hydrogen atoms of H<sub>2</sub>O adsorbed on adjacent Zn<sup>2+</sup> sites. This is also supported by the fact that  $R_{\text{Zn-OH}_2}$  increases slightly from 2.223 to 2.239 Å with the increase in H<sub>2</sub>O loading.

For the case MOF + 2H<sub>2</sub>O, the adsorption energy on the secondary site was found to be  $-0.41$  eV ( $= -39.6$  kJ/mol). It is lower than that on the primary site by ca. 0.28 eV (Table 1), indicating that the H<sub>2</sub>O adsorption is weaker on the secondary site than that on the primary. Such adsorption energy on the secondary site is still larger than the interaction energy of two H<sub>2</sub>O molecules in isolated vacuum, which is  $-0.18$  eV. This is due to the hydrogen-bonding interaction between H in H<sub>2</sub>O and O in MOF framework, as shown in Figure 1c. When a third H<sub>2</sub>O is placed near the occupied secondary site, it can also bond with H<sub>2</sub>O(1) and H<sub>2</sub>O(2), and the corresponding adsorption energy is  $-0.24$  eV, significantly lower than that for H<sub>2</sub>O(2). These negative values indicate that multiple H<sub>2</sub>O molecules can be adsorbed near the same Zn<sup>2+</sup> site and form a H<sub>2</sub>O cluster. Under higher H<sub>2</sub>O loadings, such as MOF + 19H<sub>2</sub>O and MOF + 20H<sub>2</sub>O, the adsorption energy and bonding situation are similar to those of MOF + 2H<sub>2</sub>O.

**3.2. Temperature-Dependent H<sub>2</sub>O Desorption.** Another important phenomenon in the water adsorption process is the desorption of water followed by diffusion in the pore. Although the adsorption energies are negative as discussed above, the kinetic energy of the H<sub>2</sub>O molecules would overcome the energy barrier upon temperature increase. Therefore, H<sub>2</sub>O molecules are more likely to migrate from these sites at higher temperatures; i.e., the adsorbed H<sub>2</sub>O molecules would be desorbed at high temperatures. During the desorption, the translational diffusion of adsorbed H<sub>2</sub>O is essential. Thonhauser et al.<sup>25</sup> have studied the H<sub>2</sub>O molecular diffusion in the Mg-MOF-74 structure at 0 K using the climbing-image nudged elastic band (NEB) method based on the constrained motion of single H<sub>2</sub>O within the MOF structure. In practice, however, it is known that diffusion is a complex process involving the concerted motions of many different H<sub>2</sub>O molecules. It is therefore highly desirable to study the diffusion with *ab initio* MD simulations.<sup>59</sup> Therefore, we have performed the MD simulations using the DFTB method at different temperatures and then calculated the displacements of H<sub>2</sub>O molecules as a function of time to examine this dynamic diffusion feature of the adsorbed H<sub>2</sub>O molecules.

The displacement of a H<sub>2</sub>O molecule can be defined as

$$\delta R = |R(t) - R(0)| \quad (7)$$

where  $R(t)$  is the mass center position of the molecule at time  $t$  and  $R(0)$  is its equilibrium mass center position at 0 K. The displacements of adsorbed H<sub>2</sub>O molecules on primary adsorption sites [H<sub>2</sub>O(1)] and secondary sites [H<sub>2</sub>O(2)], for MOF + 20 H<sub>2</sub>O at 150, 250, and 300 K, are shown in Figure 2a.

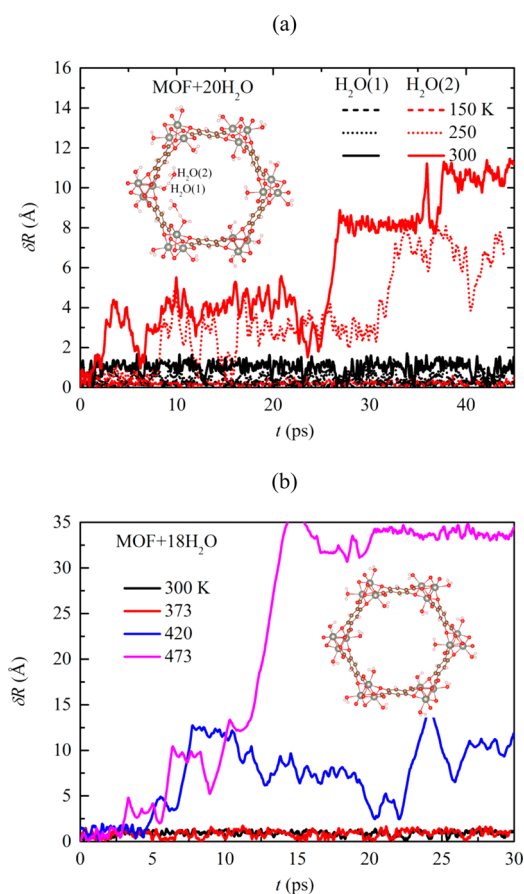


**Figure 2.** Predicted time variations of the adsorbed H<sub>2</sub>O molecule displacements (a) at the primary [H<sub>2</sub>O(1)] and secondary [H<sub>2</sub>O(2)] sites in MOF + 20H<sub>2</sub>O at 150, 250, and 300 K and (b) at the primary sites in MOF + 18H<sub>2</sub>O at 300, 373, 420, and 473 K.

At 150 K, the displacements H<sub>2</sub>O(1) and H<sub>2</sub>O(2) are nearly zero, i.e., retained the equilibrium positions. However, when the temperature increases to 250 and 300 K, the displacements of H<sub>2</sub>O(1) relative to the initial position remain almost unchanged within nearly 0.5 and 1.0 Å, respectively, indicating H<sub>2</sub>O(1) is keeping oscillating around their original sites; i.e., the primary sites are retained, while the displacements of H<sub>2</sub>O(2) undergo a few jumps from 3.0 to 7.0 as well as from 4.0 to 8.0 Å and then to 11.0 Å in 40 ps, respectively, suggesting a remarkable diffusion behavior of H<sub>2</sub>O(2) within the pore (cage) at 250 and 300 K. These suggest that at 250 and 300 K the H<sub>2</sub>O molecules on the primary sites are stable, while H<sub>2</sub>O(2) on the secondary sites will be desorbed. To shed more light on the diffusion temperature of H<sub>2</sub>O(1) molecules, Figure 2b shows the displacements of H<sub>2</sub>O(1) for MOF + 18H<sub>2</sub>O at 300, 373, 420, and 473 K. Displacements relative to the initial positions are nearly 1.0 Å at 300 and 373 K, while the displacement drastically increases at 420 and 473 K, indicating the apparent desorption of H<sub>2</sub>O(1) above 420 K. From the Redhead formula<sup>60</sup>

$$\Delta E_1 = RT_d[\ln(fT_{pd}/\beta) - \ln(\Delta E_1/RT_d)] \quad (8)$$

where  $R$ ,  $T_d$ ,  $f$ , and  $\beta$  are the gas constant, desorption temperature, desorption frequency, and heating rate, respectively. With a typical value of  $f/\beta \sim 10^8/\text{K}$  for strong bonding,<sup>61</sup> the estimated  $T_d$  for  $\text{H}_2\text{O}(1)$  and  $\text{H}_2\text{O}(2)$  are around 220 and 380 K, respectively, almost consistent with the MD predictions, although there is a deviation in value.

To verify these predictions,  $\text{H}_2\text{O}$  adsorption isotherms of Zn-MOF-74 were measured at 298 K, with the samples evacuated under vacuum (ca. 5 Pa) for 2 h between cycles (Figure 3a).

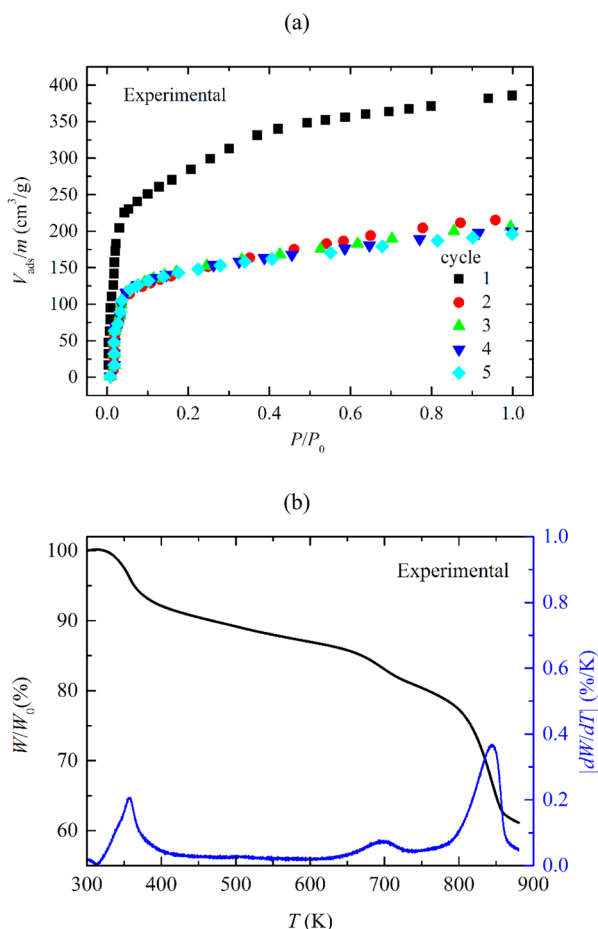


**Figure 3.** (a)  $\text{H}_2\text{O}$  adsorption isotherms for Zn-MOF-74 measured at 298 K. The sample was evacuated for 2 h at 298 K between cycles. (b) TGA trace for Zn-MOF-74 after  $\text{H}_2\text{O}$  exposure, together with its derivative with respect to temperature. A ramp rate of 5.0 K/min is used.

There is a sharp increase in the uptake in low relative pressure range in each cycle, indicating the strong binding of  $\text{H}_2\text{O}$  molecules to the micropore surface. However, there is a sudden drop of  $\text{H}_2\text{O}$  uptake after the first cycle while the  $\text{H}_2\text{O}$  adsorption isotherm curves are almost identical for the subsequent cycles. This clearly indicates the degeneration of water adsorption capacity at room temperature as also reported before.<sup>27,29</sup> When all the primary sites in a cell are occupied by  $\text{H}_2\text{O}$ , i.e., 18  $\text{H}_2\text{O}$  molecules per cell, the corresponding  $\text{H}_2\text{O}$  uptake is ca.  $140 \text{ cm}^3/\text{g}$  (ca. 11 wt %). So when all the primary and secondary adsorption sites are fully occupied, the  $\text{H}_2\text{O}$  uptake is estimated to be  $280 \text{ cm}^3/\text{g}$ . According to the Brunauer–Emmett–Teller (BET) theory,<sup>62</sup> the monolayer

$\text{H}_2\text{O}$  quantities directly adsorbed on the pore surface in the first and subsequent cycles were fitted with the experimental adsorption isotherm results, and they are 232 and  $121 \text{ cm}^3/\text{g}$ , respectively, which are only slightly smaller than the above theoretical values. To further verify these speculations, the thermogravimetric analysis (TGA) trace for Zn-MOF-74 after  $\text{H}_2\text{O}$  exposure and evacuation process at room temperature were measured, as shown in Figure 3b. The TGA curve shows a fast mass loss regime near 360 K, followed by a gradual loss in mass up to the apparent framework decomposition at around 840 K. The 11% mass loss due to  $\text{H}_2\text{O}$  desorption is observed at 360 K, indicating that 50 wt % of  $\text{H}_2\text{O}$  still remains even after the evacuation at room temperature, in good agreement with our predictions. These results therefore lead to the conclusion that at room temperature the capacity contributed by the secondary adsorption sites can be regenerated, while the desorption on the primary sites can only occur at elevated temperatures.

**3.3. Structural Stability under  $\text{H}_2\text{O}$  adsorption.** The two interactions between  $\text{H}_2\text{O}$  and the framework are (1) Zn–O bonding interaction between the O ion in  $\text{H}_2\text{O}(1)$  and the unsaturated  $\text{Zn}^{2+}$  ion and (2) H-bonding interaction between the H ions in  $\text{H}_2\text{O}(1)/\text{H}_2\text{O}(2)$  and the O ions in the MOF framework. These may influence the structural stability of Zn-MOF-74. In order to explore this structural stability under  $\text{H}_2\text{O}$  exposure, we compared the unit cell volume of empty Zn-MOF-74 and the framework under 11 wt %  $\text{H}_2\text{O}$  loading (MOF +  $18\text{H}_2\text{O}$ ) with respect to temperature using molecular dynamics simulations (Figure 4a). A period of more than 200 ps was adopted for each simulation, and the volume was averaged over time for the comparison. For empty Zn-MOF-74, the volume variations with temperature show two regimes; the volume gradually decreases by about 1.0% with the temperature from 300 to 620 K, indicating the occurrence of negative thermal expansion. When the temperature is higher than 620 K, the volume decreases sharply by 40%, indicating the structural decomposition of Zn-MOF-74 at high temperatures. Indeed, the TGA curve demonstrated significant mass loss starting from 650 K (Figure 3b).

When the framework contains water molecules (MOF +  $18\text{H}_2\text{O}$ ), the volume shrinkage below 373 K (1.3%) is slightly larger than that of guest-free Zn-MOF-74. This indicates the occluded water molecules influence the rigidity of the crystal structure of Zn-MOF-74. However, Figure 4b shows that the unit cell volume of MOF +  $18\text{H}_2\text{O}$  does not change noticeably at 300 K during the simulations, indicating structural stability of Zn-MOF-74 against water at least up to 200 ps. Above 373 K,  $\text{H}_2\text{O}$  molecules on the framework begin to desorb from the primary adsorption sites, as shown in Figure 2. Thus,  $\text{H}_2\text{O}$  molecules should not affect the structural stability at high temperatures if desorbed water molecules do not cleave the Zn–O bond of the framework. The negligible volume change of Zn-MOF-74 is supported by the PXRD pattern of Zn-MOF-74 obtained after  $\text{H}_2\text{O}$  adsorption measurements. As shown in Figure 4c, the patterns before and after  $\text{H}_2\text{O}$  exposure are nearly identical, which is reminiscent of Mg-MOF-74,<sup>63</sup> suggesting that  $\text{H}_2\text{O}$  exposure at ambient temperature does not affect the integrity of crystal structure.

It is generally thought the structural degradation or decomposition of MOF-74 under water adsorption is the cause of for its negligible nitrogen uptake at 77 K. However, based on the PXRD observations,<sup>27,63</sup> the MOF-74 remains intact after water adsorption at room temperature. It is reported

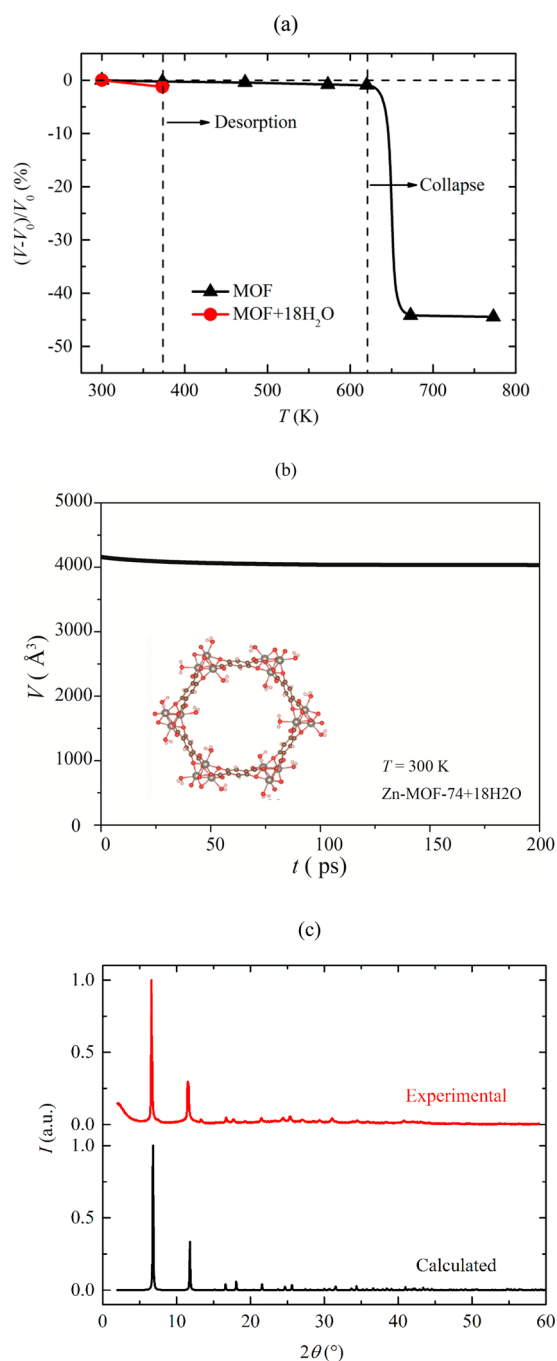


**Figure 4.** (a) Predicted variations of volume change of Zn-MOF-74, with and without adsorbed H<sub>2</sub>O, with respect to temperatures. (b) Time variation of the unit-cell volume of Zn-MOF-74 + 18H<sub>2</sub>O at 300 K. (c) Experimental powder X-ray diffraction pattern of Zn-MOF-74 after H<sub>2</sub>O exposure at 298 K. Comparison is made with the pattern calculated using the crystal structure of Zn-MOF-74.

that Mg-MOF-74 undergoes significant reduction in BET surface area (N<sub>2</sub> adsorption capacity at 77 K), i.e., 83% at 80% relative humidity<sup>27</sup> and 99% at 90% relative humidity.<sup>63</sup> However, the reduction in the NH<sub>3</sub> adsorption capacity of Mg-MOF-74 is negligible at 90% relative humidity at 298 K.<sup>63</sup> These indicate that the gas adsorption capacity in MOF-74 decreases after H<sub>2</sub>O exposure, and this reduction may be closely related to the polarity of the adsorbed gas. We measured Zn-MOF-74 adsorption isotherms for N<sub>2</sub> at 77 K and observed a sharp decrease in N<sub>2</sub> uptake, from 290 cm<sup>3</sup>/g for dry Zn-

MOF-74 to almost 0 cm<sup>3</sup>/g after the water exposure. This significant drop in N<sub>2</sub> adsorption capacity is consistent with the results of Mg-MOF-74.<sup>27,63</sup> To explain this drop in the N<sub>2</sub> adsorption capacity, the binding strengths between N<sub>2</sub> and the Zn-MOF-74 with and without H<sub>2</sub>O coordination were calculated with DFTB+. After the optimization, N<sub>2</sub> moved to the Zn<sup>2+</sup> sites in the empty Zn-MOF-74, but they would adhere to coordinated H<sub>2</sub>O in the hydrated structure since Zn<sup>2+</sup> sites are screened by H<sub>2</sub>O. The corresponding binding energies are 0.11 eV with and 0.45 eV without H<sub>2</sub>O coordination, indicating that N<sub>2</sub> adsorption is much weaker in hydrated Zn-MOF-74. Besides, the binding energy of H<sub>2</sub>O(2) is much larger compared to N<sub>2</sub> molecules with H<sub>2</sub>O(1) coordination. So the heat from N<sub>2</sub> adsorption is not large enough to break the water cluster to reach the surface of Zn-MOF-74. The water cluster formed by H<sub>2</sub>O(1) and H<sub>2</sub>O(2) in the pore may prevent the adsorption of N<sub>2</sub> molecules in Zn-MOF-74.

### 3.4. IR Spectra and Vibrational Spectroscopy Analysis.

To further study the effect of adsorbed H<sub>2</sub>O on the structure of Zn-MOF-74, the IR spectra of Zn-MOF-74 samples were measured under two conditions: (i) activated samples measured under N<sub>2</sub>, or “dry” samples, and (ii) activated samples after exposure to H<sub>2</sub>O, called “hydrated” samples. Figure 5a shows intense bands at 366, 414, 502, 549, 734, 808,

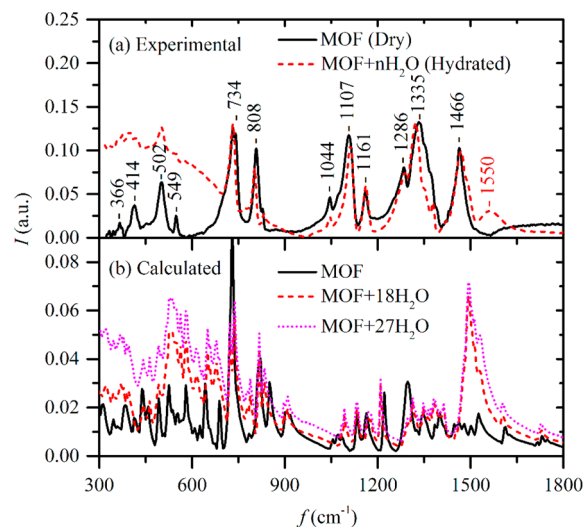


**Figure 5.** (a) Measured IR absorption spectra (arbitrary units) of dry and hydrated Zn-MOF-74. Dry: activated sample measured under N<sub>2</sub>. Hydrated: after H<sub>2</sub>O adsorption isotherm measurement. (b) Calculated IR absorption spectra (arbitrary units) of pristine and hydrated Zn-MOF-74 (MOF + 20H<sub>2</sub>O and MOF + 27H<sub>2</sub>O) at 300 K using integration time steps of 4.0 fs.

1044, 1107, 1161, 1286, 1335, and 1466 cm<sup>-1</sup> for the “dry” sample. The assignments of these bands of Zn-MOF-74 are presented in Table 2. From the literature,<sup>29,63,64</sup> the symmetric stretching mode of the bridged carbonates  $\nu_s(\text{COO}^-)$  is present at 1335 cm<sup>-1</sup>, while the asymmetric  $\beta_{as}(\text{COO}^-)$  and symmetric  $\beta_s(\text{COO}^-)$  bending modes of the bridged carbonates are located at 734 and 502 cm<sup>-1</sup>, respectively. The stretching mode of phenolic group  $\nu(\text{C}-\text{O})$  is observed in 1286 cm<sup>-1</sup>. A series of bands are associated with the aromatic ring: the band at 1466 cm<sup>-1</sup> is attributed to C–C stretching mode  $\nu(\text{C}-\text{C})_{ar}$ , the two bands at 1161 and 1107 cm<sup>-1</sup> are corresponding to the in-plane C–H bending modes  $\beta(\text{C}-\text{H})_{ip}$ , and the band at 808 cm<sup>-1</sup> is

**Table 2. Summary of Zn-MOF-74 Vibration Mode (Vibration Peak) Changes after Hydration**

MOF vibration mode	dry peak ( $\text{cm}^{-1}$ )	peak shift ( $\text{cm}^{-1}$ )
$f(\text{C}-\text{C})_{\text{ar}}$	1466	+2
$f_s(\text{COO}^-)$	1335	-12
$f(\text{C}-\text{O})$	1286	+2
$\beta(\text{C}-\text{H})_{\text{ip}}$	1161	0
$\beta(\text{C}-\text{H})_{\text{ip}}$	1107	+5
$\beta(\text{C}-\text{H})_{\text{oop}}$	808	-5
$\beta_{\text{as}}(\text{COO}^-)$	734	-2
$\beta_s(\text{COO}^-)$	502	-2

corresponding to the out-of-plane modes  $\beta(\text{C}-\text{H})_{\text{oop}}$ . The other bands will be discussed along with the VDOS.

Changes in the IR spectrum under  $\text{H}_2\text{O}$  adsorption are minimal. There is no loss of bands in the virgin sample, and only small shifts in some bands are observed (listed in Table 2), indicating that there is no obvious change in the structure of Zn-MOF-74 after  $\text{H}_2\text{O}$  exposure. Compared to the “dry” sample, there is an additional band at  $1566 \text{ cm}^{-1}$  for the “hydrated” sample, corresponding to the angular bending vibration of  $\text{H}_2\text{O}$ . Also, the intensity of the bands between 300 and  $750 \text{ cm}^{-1}$  increases, which may be due to free  $\text{H}_2\text{O}$  molecules.

The substrate contribution is large in the IR measurement, and the most intense bands cannot be correctly registered due to instrumental limitations.<sup>64,65</sup> To further analyze the vibrations, we calculated the IR spectrum of dry and hydrated Zn-MOF-74 ( $\text{MOF} + 20\text{H}_2\text{O}$  and  $\text{MOF} + 27\text{H}_2\text{O}$ ) with DFTB at 300 K, with the integration time step of 4.0 fs, as shown in Figure 5b. The calculated peaks of the dry Zn-MOF-74 agree well with the experiments, while the magnitudes differ. When the  $\text{H}_2\text{O}$  content in a cell increases from 18 to 27  $\text{H}_2\text{O}$ , i.e., more free  $\text{H}_2\text{O}$  molecules exist in the framework, the bands between 300 and  $750 \text{ cm}^{-1}$  become broadened and their intensities increase, which confirms the enhanced IR absorption in this region in the “hydrated” sample is due to free  $\text{H}_2\text{O}$  in the sample.

To further verify the IR bands and analyze the interactions between Zn-MOF-74 and the adsorbed  $\text{H}_2\text{O}$  molecules, we calculated the partial VDOS of Zn-MOF-74 and  $\text{MOF} + 20\text{H}_2\text{O}$  at 300 K, with an integration time step of 4.0 fs, as shown in Figure 6a. Contributions of the bonds involving hydrogen atoms are dominant in the energy range shown. Very strong bands are observed at 809, 1118, 1215, and  $3098 \text{ cm}^{-1}$  in Zn-MOF-74, corresponding to the C–H out-of-plane bending, in-plane bending, and stretching modes in the aromatic ring, respectively. Compared to the experimental IR spectra, the C–H out-of-plane and in-plane bending are larger in energy (blue shift) by 1, 11, and  $54 \text{ cm}^{-1}$ . A broad band centered at  $128 \text{ cm}^{-1}$  is associated with the Zn–O modes. A broad band region ( $300\text{--}1400 \text{ cm}^{-1}$ ) mainly arises from the C–O modes. The C–C modes in this case were observed at  $1500\text{--}1800 \text{ cm}^{-1}$ . Comparing the partial VDOS of the Zn-MOF-74 with  $\text{MOF} + 20\text{H}_2\text{O}$ , there are slight shifts in some bands. Also, three prominent bands at 1503, 3500, and  $3904 \text{ cm}^{-1}$  are present in the  $\text{MOF} + 20\text{H}_2\text{O}$  (and not in the Zn-MOF-74), corresponding to the H–O–H bending  $\beta(\text{H}-\text{O}-\text{H})$ , symmetric H–O  $\nu_s(\text{H}-\text{O})$ , and antisymmetric  $\nu_{\text{as}}(\text{H}-\text{O})$  H–O stretching modes of  $\text{H}_2\text{O}$ . Other fine distinction would be observed in Figure 6b.

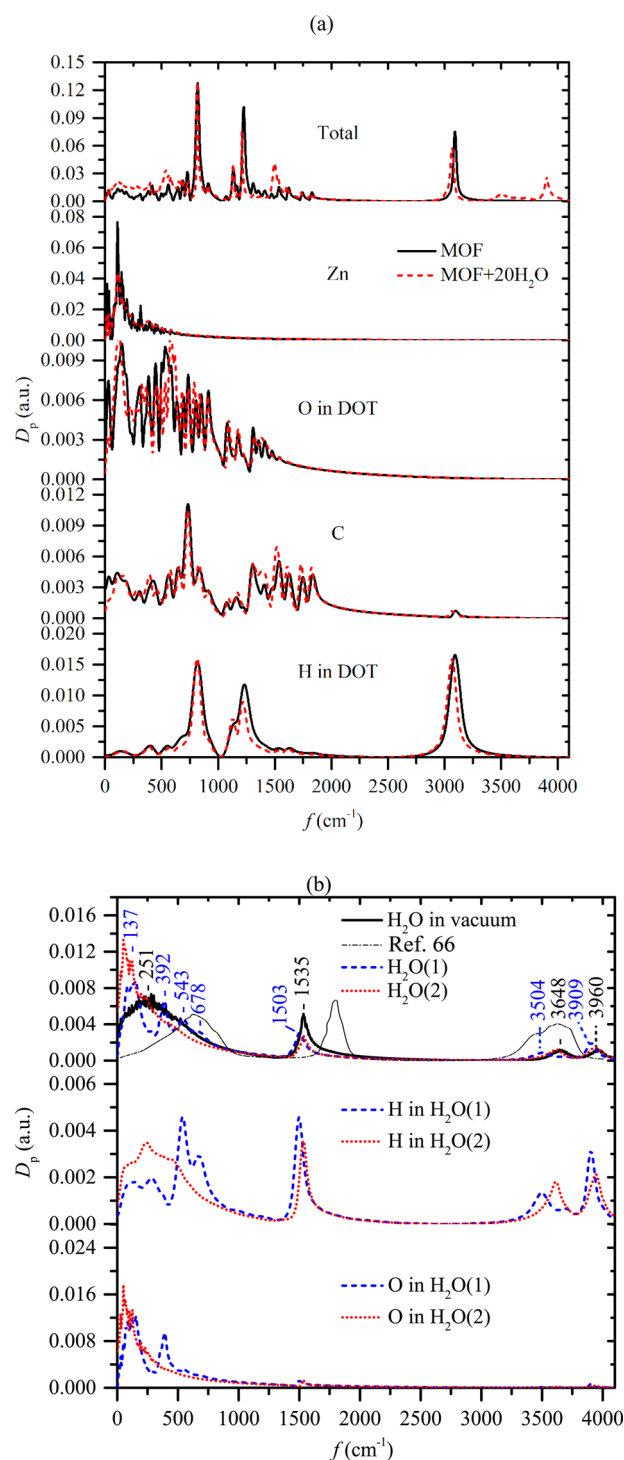


**Figure 6.** Calculated VDOS (arbitrary units) of (a) pristine Zn-MOF-74 and hydrated Zn-MOF-74 ( $\text{MOF} + 20\text{H}_2\text{O}$ ) and (b)  $\text{H}_2\text{O}$  molecules in vacuum and in  $\text{MOF} + 20\text{H}_2\text{O}$  at 300 K using integration time steps of 4.0 fs. Various vibrational peaks are marked, including their shifts under water adsorption. The vibrational spectrum of water calculated by classical molecular dynamics<sup>66</sup> is also shown.

To further test whether the frequency shift of  $\text{H}_2\text{O}$  can be affected by the adsorption sites, we have also performed a MD simulation for liquid water with 20  $\text{H}_2\text{O}$  molecules at 300 K in an isolated system to obtain the VDOS of liquid water molecules ( $\text{H}_2\text{O}$  in vacuum). With more molecules considered, the sharp peaks will be further smeared out. Figure 6b shows

the VDOS of liquid H<sub>2</sub>O molecules. The overall vibrational spectrum shows typical characteristics of condensed H<sub>2</sub>O systems, i.e., a few broad smearing bands in the low-frequency regime (<800 cm<sup>-1</sup>). Four characteristic bands are observed for liquid H<sub>2</sub>O. The broad band centered on 251 cm<sup>-1</sup> corresponds to the rotating modes. A sharp peak around 1535 cm<sup>-1</sup> is produced by the bending modes of the H<sub>2</sub>O molecules, which cannot be found in the VDOS of the MOF structure. The sharp peaks at 3648 and 3960 cm<sup>-1</sup> correspond to the symmetric and antisymmetric stretching modes of H<sub>2</sub>O molecules, respectively. These modes are strongly affected by the hydrogen bonding. The comparison with the vibrational spectrum calculated by classical molecular dynamics with a system of 2048 SPC water molecules<sup>66</sup> is also shown, and overall a reasonable agreement is found, although the bending frequency calculated by DFTB is closer to the experimental value. The bending and symmetric stretching modes of H<sub>2</sub>O molecules are lower in energy (red-shift) by -8 and -60 cm<sup>-1</sup> with respect to the positions determined experimentally.<sup>29</sup> But the antisymmetric stretching mode is blue-shift to a larger extent (+181 cm<sup>-1</sup>).

The VDOS of H<sub>2</sub>O molecules in the Zn-MOF-74 [H<sub>2</sub>O(1) and H<sub>2</sub>O(2)] are also shown in Figure 6b and compared with that of liquid H<sub>2</sub>O. The high-frequency vibration modes for the three types of H<sub>2</sub>O molecules are very similar since they are related to intramolecular motions. Overall, the bands of H<sub>2</sub>O(2) are very similar to those of free H<sub>2</sub>O molecules in vacuum. As shown in Table 3, there is a slight red-shift relative

**Table 3. Summary of H<sub>2</sub>O Vibration Mode (Peak) Changes in Zn-MOF-74 and Relation to Free H<sub>2</sub>O Vibration**

H <sub>2</sub> O vibration mode	peak in free H <sub>2</sub> O (cm <sup>-1</sup> )	peak shift (cm <sup>-1</sup> )	
		H <sub>2</sub> O(1)	H <sub>2</sub> O(2)
<i>f</i> <sub>as</sub> (H-O)	3960	-51	-23
<i>f</i> <sub>s</sub> (H-O)	3648	-144	-28
<i>β</i> (H-O-H)	1535	-32	-2

to free H<sub>2</sub>O (the bending, symmetric, and antisymmetric stretching modes red-shift by -2, -28, and -23 cm<sup>-1</sup>), indicating H<sub>2</sub>O(2) molecules is closed to free H<sub>2</sub>O states in the Zn-MOF-74 at 300 K. This is reasonable since H<sub>2</sub>O(2) is desorbed from the Zn sites at 300 K and becomes relatively free. H<sub>2</sub>O(1) molecules, however, have sharp peaks at 137, 392, 543, and 678 cm<sup>-1</sup> in the low-frequency regime, corresponding to the interactions between O in H<sub>2</sub>O(1) and Zn in MOF and those between H in H<sub>2</sub>O(1) and O in Zn-MOF-74. For H<sub>2</sub>O(1) molecules, the bending, symmetric and antisymmetric stretching modes also undergo red-shift (-32, -144, and -51 cm<sup>-1</sup>) to 1503, 3504, and 3909 cm<sup>-1</sup>, respectively (see Table 3). These shifts are mainly due to the hydrogen-bonding interactions between MOF and H<sub>2</sub>O.

The lattice dynamics affects the thermal transport and in a separate communication we will report on the anisotropic lattice thermal conductivity of Zn-MOF-74 (lattice thermal conductivity of MOF-5 was addressed in refs 65 and 67).

#### 4. CONCLUSIONS

We have investigated H<sub>2</sub>O adsorption/desorption in Zn-MOF-74 and their effects on the lattice structure using MD based on DFT with the tight-binding approximation (DFTB) and also experiments. The predicted absorption energies from DFTB are in good agreement with vdW-DFT, validating DFTB

suitable to investigate absorption properties, where *ab initio* quantum chemistry calculations are prohibitive. It is found that there exist both a primary and a secondary adsorption sites near the Zn<sup>2+</sup> position and multiple H<sub>2</sub>O molecules may be adsorbed near the same Zn<sup>2+</sup> site, making it possible to form H<sub>2</sub>O clusters at low temperatures. We have identified two types of adsorbed H<sub>2</sub>O, i.e., coordinated H<sub>2</sub>O on the primary adsorption sites and H-bonded H<sub>2</sub>O on the secondary sites, having different adsorption/desorption properties. The adsorption energy of the coordinated H<sub>2</sub>O (ca. 0.7 eV) is larger than the H-bonded H<sub>2</sub>O (ca. 0.4 eV), resulting in a higher desorption temperature, which is the main reason for the degradation of H<sub>2</sub>O uptake from the first to the following isotherm cycles. We also show that Zn-MOF-74 structure remains stable with 10 wt % H<sub>2</sub>O uptake (MOF + 18H<sub>2</sub>O) below 573 K, making it promising for heat transformation applications, although the regeneration should be conducted at a relatively high temperature. The vibration states of the MOF-74 lattice and H<sub>2</sub>O molecules during the adsorption process have also been clarified.

#### AUTHOR INFORMATION

##### Corresponding Author

\*E-mail: mebh Huang@ust.hk (B.H.).

##### Notes

The authors declare no competing financial interest.

#### ACKNOWLEDGMENTS

The experimental data and fruitful discussions with H. Furukawa, Y. B. Zhang, and O. Yaghi of UC Berkeley are greatly appreciated. Y.L. and B.H. are grateful for the support from the Hong Kong General Research Fund (Grant No. 613211) and National Natural Science Foundation of China (Grant No. 51376154). J.D.C. and M.K. are thankful for support by Energy Efficiency & Resources (Award No. 20122010100120) of Korea Institute of Energy Technology Evaluation and Planning funded by Ministry of Knowledge Economy. The computing service provided by the National Supercomputer Center, Tianjin, China, is appreciated.

#### REFERENCES

- (1) Tan, K.; Zuluaga, S.; Gong, Q.; Canepa, P.; Wang, H.; Li, J.; Chabal, Y. J.; Thonhauser, T. Water Reaction Mechanism in Metal Organic Frameworks with Coordinatively Unsaturated Metal Ions: MOF-74. *Chem. Mater.* **2014**, *26*, 6886–6895.
- (2) Jänchen, J.; Ackermann, D.; Stach, H.; Brösicke, W. Studies of the Water Adsorption on Zeolites and Modified Mesoporous Materials for Seasonal Storage of Solar Heat. *Sol. Energy* **2004**, *76*, 339–344.
- (3) Henninger, S. K.; Schmidt, F. P.; Henning, H. M. Water Adsorption Characteristics of Novel Materials for Heat Transformation Applications. *Appl. Therm. Eng.* **2010**, *30*, 1692–1702.
- (4) Ehrenmann, J.; Henninger, S. K.; Janiak, C. Water Adsorption Characteristics of MIL-101 for Heat-Transformation Applications of Mofs. *Eur. J. Inorg. Chem.* **2011**, *2011*, 471–474.
- (5) Jeremias, F.; Frohlich, D.; Janiak, C.; Henninger, S. K. Water and Methanol Adsorption on MOFs for Cycling Heat Transformation Processes. *New J. Chem.* **2014**, *38*, 1846–1852.
- (6) Henninger, S. K.; Jeremias, F.; Kummer, H.; Janiak, C. MOFs for Use in Adsorption Heat Pump Processes. *Eur. J. Inorg. Chem.* **2012**, *2012*, 2625–2634.
- (7) Demir, H.; Mobedi, M.; Ülkü, S. A Review on Adsorption Heat Pump: Problems and Solutions. *Renewable Sustainable Energy Rev.* **2008**, *12*, 2381–2403.

- (8) Ng, E. P.; Mintova, S. Nanoporous Materials with Enhanced Hydrophilicity and High Water Sorption Capacity. *Microporous Mesoporous Mater.* **2008**, *114*, 1–26.
- (9) Khutia, A.; Rammelberg, H. U.; Schmidt, T.; Henninger, S.; Janiak, C. Water Sorption Cycle Measurements on Functionalized MIL-101Cr for Heat Transformation Application. *Chem. Mater.* **2013**, *25*, 790–798.
- (10) Seo, Y.-K.; et al. Energy-Efficient Dehumidification over Hierarchically Porous Metal–Organic Frameworks as Advanced Water Adsorbents. *Adv. Mater.* **2012**, *24*, 806–810.
- (11) Furukawa, H.; Cordova, K. E.; O’Keeffe, M.; Yaghi, O. M. The Chemistry and Applications of Metal–Organic Frameworks. *Science* **2013**, *341*, 1230444.
- (12) Zhou, H.-C.; Long, J. R.; Yaghi, O. M. Introduction to Metal–Organic Frameworks. *Chem. Rev.* **2012**, *112*, 673–674.
- (13) Furukawa, H.; et al. Ultrahigh Porosity in Metal–Organic Frameworks. *Science* **2010**, *329*, 424–428.
- (14) Mason, J. A.; Veenstra, M.; Long, J. R. Evaluating Metal–Organic Frameworks for Natural Gas Storage. *Chem. Sci.* **2014**, *5*, 32–51.
- (15) Nugent, P.; et al. Porous Materials with Optimal Adsorption Thermodynamics and Kinetics for CO<sub>2</sub> Separation. *Nature* **2013**, *495*, 80–84.
- (16) Sumida, K.; Rogow, D. L.; Mason, J. A.; McDonald, T. M.; Bloch, E. D.; Herm, Z. R.; Bae, T.-H.; Long, J. R. Carbon Dioxide Capture in Metal–Organic Frameworks. *Chem. Rev.* **2011**, *112*, 724–781.
- (17) Britt, D.; Furukawa, H.; Wang, B.; Glover, T. G.; Yaghi, O. M. Highly Efficient Separation of Carbon Dioxide by a Metal–Organic Framework Replete with Open Metal Sites. *Proc. Natl. Acad. Sci. U. S. A.* **2009**, *106*, 20637–20640.
- (18) Achmann, S.; Hagen, G.; Hämmerle, M.; Malkowsky, I. M.; Kiener, C.; Moos, R. Sulfur Removal from Low-Sulfur Gasoline and Diesel Fuel by Metal–Organic Frameworks. *Chem. Eng. Technol.* **2010**, *33*, 275–280.
- (19) Li, J. R.; Kuppler, R. J.; Zhou, H. C. Selective Gas Adsorption and Separation in Metal–Organic Frameworks. *Chem. Soc. Rev.* **2009**, *38*, 1477–1504.
- (20) Low, J. J.; Benin, A. I.; Jakubczak, P.; Abrahamian, J. F.; Faheem, S. A.; Willis, R. R. Virtual High Throughput Screening Confirmed Experimentally: Porous Coordination Polymer Hydration. *J. Am. Chem. Soc.* **2009**, *131*, 15834–15842.
- (21) Cychoz, K. A.; Matzger, A. J. Water Stability of Microporous Coordination Polymers and the Adsorption of Pharmaceuticals from Water. *Langmuir* **2010**, *26*, 17198–17202.
- (22) Saha, D.; Deng, S. Structural Stability of Metal Organic Framework MOF-177. *J. Phys. Chem. Lett.* **2009**, *1*, 73–78.
- (23) Greathouse, J. A.; Allendorf, M. D. The Interaction of Water with MOF-5 Simulated by Molecular Dynamics. *J. Am. Chem. Soc.* **2006**, *128*, 10678–10679.
- (24) Britt, D.; Tranchemontagne, D.; Yaghi, O. M. Metal–Organic Frameworks with High Capacity and Selectivity for Harmful Gases. *Proc. Natl. Acad. Sci. U. S. A.* **2008**, *105*, 11623–11627.
- (25) Canepa, P.; Nijem, N.; Chabal, Y. J.; Thonhauser, T. Diffusion of Small Molecules in Metal Organic Framework Materials. *Phys. Rev. Lett.* **2013**, *110*, 0261021–10.
- (26) Furukawa, H.; Gándara, F.; Zhang, Y. B.; Jiang, J.; Queen, W. L.; Hudson, M. R.; Yaghi, O. M. Water Adsorption in Porous Metal–Organic Frameworks and Related Materials. *J. Am. Chem. Soc.* **2014**, *136*, 4369–4381.
- (27) Schoenecker, P. M.; Carson, C. G.; Jasuja, H.; Flemming, C. J. J.; Walton, K. S. Effect of Water Adsorption on Retention of Structure and Surface Area of Metal–Organic Frameworks. *Ind. Eng. Chem. Res.* **2012**, *51*, 6513–6519.
- (28) Liu, J.; Wang, Y.; Benin, A. I.; Jakubczak, P.; Willis, R. R.; LeVan, M. D. CO<sub>2</sub>/H<sub>2</sub>O Adsorption Equilibrium and Rates on Metal–Organic Frameworks: HKUST-1 and Ni/DOBDC. *Langmuir* **2010**, *26*, 14301–14307.
- (29) Hadjiivanov, K. I.; Vayssilov, G. N. Characterization of Oxide Surfaces and Zeolites by Carbon Monoxide as an IR Probe Molecule. *Adv. Catal.* **2002**, *47*, 307–511.
- (30) Grant Glover, T.; Peterson, G. W.; Schindler, B. J.; Britt, D.; Yaghi, O. MOF-74 Building Unit Has a Direct Impact on Toxic Gas Adsorption. *Chem. Eng. Sci.* **2011**, *66*, 163–170.
- (31) Han, S. S.; Choi, S.-H.; van Duin, A. C. T. Molecular Dynamics Simulations of Stability of Metal–Organic Frameworks against H<sub>2</sub>O Using the REAXFF Reactive Force Field. *Chem. Commun.* **2010**, *46*, 5713–5715.
- (32) Aradi, B.; Hourahine, B.; Frauenheim, T. DFTB+, a Sparse Matrix-Based Implementation of the DFTB Method. *J. Phys. Chem. A* **2007**, *111*, 5678–5684.
- (33) Hohenberg, P.; Kohn, W. Inhomogeneous Electron Gas. *Phys. Rev.* **1964**, *136*, B864–B871.
- (34) Kohn, W.; Sham, L. J. Self-Consistent Equations Including Exchange and Correlation Effects. *Phys. Rev.* **1965**, *140*, A1133–A1138.
- (35) Slater, J. C.; Koster, G. F. Simplified LCAO Method for the Periodic Potential Problem. *Phys. Rev.* **1954**, *94*, 1498–1524.
- (36) Elstner, M.; Porezag, D.; Jungnickel, G.; Elsner, J.; Haugk, M.; Frauenheim, T.; Suhai, S.; Seifert, G. Self-Consistent-Charge Density-Functional Tight-Binding Method for Simulations of Complex Materials Properties. *Phys. Rev. B* **1998**, *58*, 7260–7268.
- (37) Elstner, M.; Frauenheim, T.; Kaxiras, E.; Seifert, G.; Suhai, S. A Self-Consistent Charge Density-Functional Based Tight-Binding Scheme for Large Biomolecules. *Phys. Status Solidi B* **2000**, *217*, 357–376.
- (38) Frauenheim, T.; Seifert, G.; Elstner, M.; Hajnal, Z.; Jungnickel, G.; Porezag, D.; Suhai, S.; Scholz, R. A Self-Consistent Charge Density-Functional Based Tight-Binding Method for Predictive Materials Simulations in Physics, Chemistry and Biology. *Phys. Status Solidi B* **2000**, *217*, 41–62.
- (39) Frauenheim, T.; Seifert, G.; Elstner, M.; Niehaus, T.; Köhler, C.; Amkreutz, M.; Sternberg, M.; Hajnal, Z.; Carlo, A. D.; Suhai, S. Atomistic Simulations of Complex Materials: Ground-State and Excited-State Properties. *J. Phys.: Condens. Matter* **2002**, *14*, 3015.
- (40) Elstner, M.; Frauenheim, T.; Suhai, S. An Approximate Dft Method for QM/MM Simulations of Biological Structures and Processes. *J. Mol. Struct.: THEOCHEM* **2003**, *632*, 29–41.
- (41) Moreira, N. H.; Dolgonos, G.; Aradi, B.; da Rosa, A. L.; Frauenheim, T. Toward an Accurate Density-Functional Tight-Binding Description of Zinc-Containing Compounds. *J. Chem. Theory Comput.* **2009**, *5*, 605–614.
- (42) Zhechkov, L.; Heine, T.; Patchkovskii, S.; Seifert, G.; Duarte, H. A. An Efficient a Posteriori Treatment for Dispersion Interaction in Density-Functional-Based Tight Binding. *J. Chem. Theory Comput.* **2005**, *1*, 841–847.
- (43) Verlet, L. Computer “Experiments” on Classical Fluids. I. Thermodynamical Properties of Lennard-Jones Molecules. *Phys. Rev.* **1967**, *159*, 98–103.
- (44) Verlet, L. Computer “Experiments” on Classical Fluids. II. Equilibrium Correlation Functions. *Phys. Rev.* **1968**, *165*, 201–214.
- (45) Dion, M.; Rydberg, H.; Schröder, E.; Langreth, D. C.; Lundqvist, B. I. Van Der Waals Density Functional for General Geometries. *Phys. Rev. Lett.* **2004**, *92*, 246401.
- (46) Klimeš, J.; Bowler, D. R.; Michaelides, A. Chemical Accuracy for the Van Der Waals Density Functional. *J. Phys.: Condens. Matter* **2010**, *22*, 022201.
- (47) Klimeš, J.; Bowler, D. R.; Michaelides, A. Van Der Waals Density Functionals Applied to Solids. *Phys. Rev. B* **2011**, *83*, 195131.
- (48) Kresse, G.; Furthmüller, J. Efficient Iterative Schemes for Ab Initio Total-Energy Calculations Using a Plane-Wave Basis Set. *Phys. Rev. B* **1996**, *54*, 11169–11186.
- (49) Kresse, G.; Furthmüller, J. Efficiency of Ab-Initio Total Energy Calculations for Metals and Semiconductors Using a Plane-Wave Basis Set. *Comput. Mater. Sci.* **1996**, *6*, 15–50.

(50) Kresse, G.; Joubert, D. From Ultrasoft Pseudopotentials to the Projector Augmented-Wave Method. *Phys. Rev. B* **1999**, *59*, 1758–1775.

(51) Nijem, N.; et al. Water Cluster Confinement and Methane Adsorption in the Hydrophobic Cavities of a Fluorinated Metal–Organic Framework. *J. Am. Chem. Soc.* **2013**, *135*, 12615–12626.

(52) Fu, C. L.; Ho, K. M. First-Principles Calculation of the Equilibrium Ground-State Properties of Transition Metals: Applications to Nb and Mo. *Phys. Rev. B* **1983**, *28*, 5480–5486.

(53) Rosi, N. L.; Kim, J.; Eddaoudi, M.; Chen, B.; O’Keeffe, M.; Yaghi, O. M. Rod Packings and Metal–Organic Frameworks Constructed from Rod-Shaped Secondary Building Units. *J. Am. Chem. Soc.* **2005**, *127*, 1504–1518.

(54) Praprotnik, M.; Janežič, D. Molecular Dynamics Integration and Molecular Vibrational Theory. III. The Infrared Spectrum of Water. *J. Chem. Phys.* **2005**, *122*, 174103–10.

(55) Lopez, M. G.; Canepa, P.; Thonhauser, T. NMR Study of Small Molecule Adsorption in MOF-74-Mg. *J. Chem. Phys.* **2013**, *138*, 154704.

(56) Dietzel, P. D. C.; Johnsen, R. E.; Blom, R.; Fjellvåg, H. Structural Changes and Coordinatively Unsaturated Metal Atoms on Dehydration of Honeycomb Analogous Microporous Metal–Organic Frameworks. *Chem.—Eur. J.* **2008**, *14*, 2389–2397.

(57) Canepa, P.; Tan, K.; Du, Y.; Lu, H.; Chabal, Y. J.; Thonhauser, T. Structural, Elastic, Thermal, and Electronic Responses of Small-Molecule-Loaded Metal–Organic Framework Materials. *J. Mater. Chem. A* **2015**, *3*, 986–995.

(58) Coudert, F.-X.; Fuchs, A. H.; Neimark, A. V. Comment on “Volume Shrinkage of a Metal–Organic Framework Host Induced by the Dispersive Attraction of Guest Gas Molecules”. *Phys. Chem. Chem. Phys.* **2014**, *16*, 4394–4395.

(59) Ouyang, C.; Shi, S.; Wang, Z.; Huang, X.; Chen, L. First-Principles Study of Li Ion Diffusion in LiFePO<sub>4</sub>. *Phys. Rev. B* **2004**, *69*, 104303.

(60) Redhead, P. A. Thermal Desorption of Gases. *Vacuum* **1962**, *12*, 203–211.

(61) Joseph, Y.; Ranke, W.; Weiss, W. Water on FeO(111) and Fe<sub>3</sub>O<sub>4</sub>(111): Adsorption Behavior on Different Surface Terminations. *J. Phys. Chem. B* **2000**, *104*, 3224–3236.

(62) Brunauer, S.; Emmett, P. H.; Teller, E. Adsorption of Gases in Multimolecular Layers. *J. Am. Chem. Soc.* **1938**, *60*, 309–319.

(63) DeCoste, J. B.; Peterson, G. W.; Schindler, B. J.; Killips, K. L.; Browe, M. A.; Mahle, J. J. The Effect of Water Adsorption on the Structure of the Carboxylate Containing Metal–Organic Frameworks Cu-Btc, Mg-MOF-74, and UIO-66. *J. Mater. Chem. A* **2013**, *1*, 11922–11932.

(64) Drenchev, N.; Ivanova, E.; Mihaylov, M.; Hadjiivanov, K. Co as an Ir Probe Molecule for Characterization of Copper Ions in a Basolite C300 MOF Sample. *Phys. Chem. Chem. Phys.* **2010**, *12*, 6423–6427.

(65) Huang, B. L.; McGaughey, A. J. H.; Kaviany, M. Thermal Conductivity of Metal–Organic Framework 5 (MOF-5): Part I. Molecular Dynamics Simulations. *Int. J. Heat Mass Transfer* **2007**, *50*, 393–404.

(66) Benjamin, I. Vibrational-Spectrum of Water at the Liquid/Vapor Interface. *Phys. Rev. Lett.* **1994**, *73*, 2083–2086.

(67) Huang, B. L.; Ni, Z.; Millward, A.; McGaughey, A. J. H.; Uher, C.; Kaviany, M.; Yaghi, O. Thermal Conductivity of a Metal–Organic Framework (MOF-5): Part II. Measurement. *Int. J. Heat Mass Transfer* **2007**, *50*, 405–411.